Design Principles for Grain Boundaries in Solid-State Lithium-Ion Conductors

James A. Quirk*,† and James A. Dawson*,†,‡

†*Chemistry – School of Natural and Environmental Sciences, Newcastle University, Newcastle upon Tyne, NE1 7RU, UK*

‡*Centre for Energy, Newcastle University, Newcastle upon Tyne, NE1 7RU, UK*

E-mail: james.quirk@newcastle.ac.uk; james.dawson@newcastle.ac.uk

Abstract

Although polycrystalline solid electrolytes are central to the utilization of solid-state batteries with lithium metal anodes, lithium dendrite formation and reduced Li-ion conductivity at their grain boundaries remain primary concerns. Given that the interpretation of the results of experimental studies on polycrystalline materials can be difficult, computational techniques are invaluable for providing insight at the atomic scale. Here, we carry out first-principles calculations on representative grain boundaries in three important Li-based solid electrolyte families, namely, an anti-perovskite oxide, Li_3OCl, and its hydrated counterpart, Li_2OHCl, a thiophosphate, Li_3PS_4, and a halide, Li_3InCl_6, to demonstrate the significantly different impacts that grain boundaries have on their electronic structure, ion conductivity and correlated ion transport. Our results show that even when grain boundaries do not significantly impact ionic conductivity, they can still strongly perturb the electronic structure and contribute to undesirable electrical conductivity and potential lithium dendrite propagation. We also illustrate, for the first time, how correlated motion, including the so-called paddle-wheel mechanism, which has so far only been considered for the bulk, can vary substantially at grain boundaries. Our findings reveal the dramatically different behaviour of solid electrolytes at the grain boundary compared to the bulk and its potential consequences and benefits for the design of solid-state batteries.

Introduction

Solid-state lithium-ion batteries promise high energy density and excellent safety but there are many challenges to overcome before these goals can be realised. Crucial to the operation of solid-state batteries is the solid electrolyte, which must be able to compete with more traditional liquid electrolytes with regards to ionic conductivity.[1–5] Solid electrolytes are often produced through the sintering of powders, yielding structures in which grain boundaries (GBs) are highly prevalent.[6,7] GBs should be expected to have profound impacts on the performance of a device throughout its lifetime, some of which can be positive, such as the observed increase in ionic conductivity of Li_3PS_4 containing nanosized grains.[8] However, GBs are generally considered to be performance bottlenecks in solid electrolytes and can cause decreased ionic conductivity[9,10] and even device failure through the propagation of lithium dendrites, leading to short circuits.[11,12]

Clearly, an in-depth understanding of the impact of GBs on solid electrolytes is essential, but given that there is a huge variety of candidate electrolyte materials,[13–15] this is a not a trivial feat. The problem is further complicated by the fact that the interpretation of experimental results for polycrystalline materials can be difficult, which makes computational techniques invaluable for providing insight at the atomic scale. Despite this fact, there is currently an alarming lack of atomistic computational studies of GBs and their effects in solid electrolytes, particularly regarding their impact on electronic structure. Some progress has been made regarding ion transport at solid electrolytes GBs using molecular dynamics studies with classical potentials.[10,16–20] For example, it has been established why oxide-based solid electrolytes generally exhibit higher GB resistance[16] than sulfides and how GBs provide an explanation for the often observed differences in calculated and experimental Li-ion conductivities in some solid electrolyte families.[10] Although classical models are valuable as their low computational expense enables the investigation of large grain boundaries and nanostructures containing many tens or even hundreds of thousands of atoms over long timescales, their utility is limited by the fact that they lack access to electronic properties. Electronic properties are of increasing interest in the fields of solid electrolytes and solid-state batteries as it is these properties that underpin undesirable electrical conductivity and, especially at GBs, dendrite formation.[11,21]

In this study, we utilize first-principles calculations to elucidate how GBs impact the performance and properties of four archetypal solid electrolyte materials, namely, an oxide-based anti-perovskite (Li_3OCl)[22,23] and its hydrated counterpart (Li_2OHCl), a thiophosphate (β-Li_3PS_4)[8] and a halide (Li_3InCl_6).[24,25] The GBs in all four materials are found to exhibit narrowed band gaps and charge-trapping states that would be conducive to unwanted electronic conductivity via polaron hopping and potential dendrite formation. By comparing the results of ab-initio molecular dynamics (AIMD) simulations on the bulk and GBs of each material, it is found that the Li_3OCl GBs pose large barriers to ionic conductivity whereas the GBs in Li_2OHCl, Li_3PS_4 and Li_3InCl_6 are comparatively benign. While the contrast between GB resistance in oxides and sulfides is generally accepted, this study is the first to demonstrate the nature and origin of GB resistance in a halide-based solid electrolyte. We also show the significant influence that GBs have on correlated Li-ion transport for the first time. Our results provide design principles and important considerations for the synthesis and doping of solid electrolyte materials with high ionic and low electronic conductivity.

Results and discussion

Grain Boundary Models

Stable GB structures are shown in Figures 1a-d and were determined using the methodology outlined in the Computational Methods section which has been shown to be predictive of experimentally observed grain boundaries.[26–28] Due to the large computational cost that would be incurred by very large grain boundary models, we aim to include no more than 400 atoms in our calculations. We choose tilt angles that allow for supercell lattice vectors of at least 10 Å parallel to the GB plane whilst maintaining grains around 15 Å thick. The formation energies (Figure 1e) for all of the considered GBs are low (0.25-0.63 Jm^{-2}). The Li_3OCl GBs have been modelled previously (with a mirror-symmetric geometry rather than with any optimized rigid-body translation as in this study) using classical potentials,[10] where they were also found to have low formation energies. There have been no previous atomistic studies of GBs in Li_2OHCl, Li_3PS_4 or Li_3InCl_6, but the low formation energies indicate that our models are reasonable and representative. Such low formation energies also imply that these GBs would be prevalent throughout the materials in equilibrium conditions, further highlighting the critical importance of the role they play in device performance.

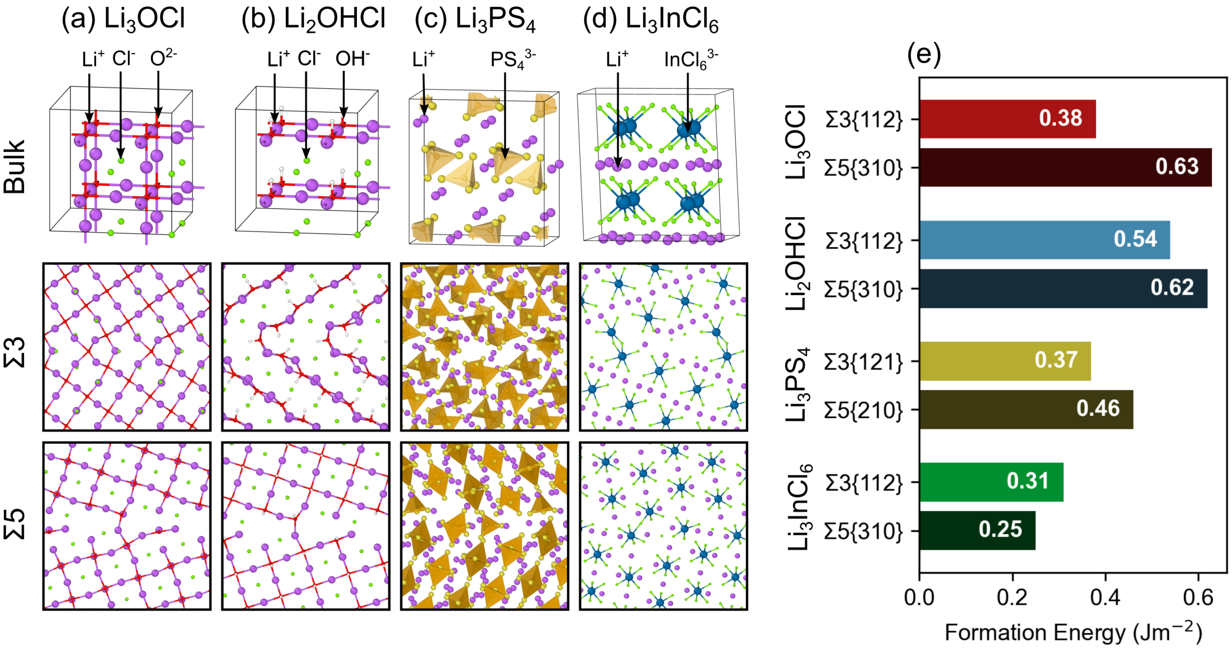

Figure 1: Structural models of the bulk and Σ3 and Σ5 GBs of (a) Li_3OCl, (b) Li_2OHCl, (c) Li_3PS_4 and (d) Li_3InCl_6. (e) Formation energy for each GB.

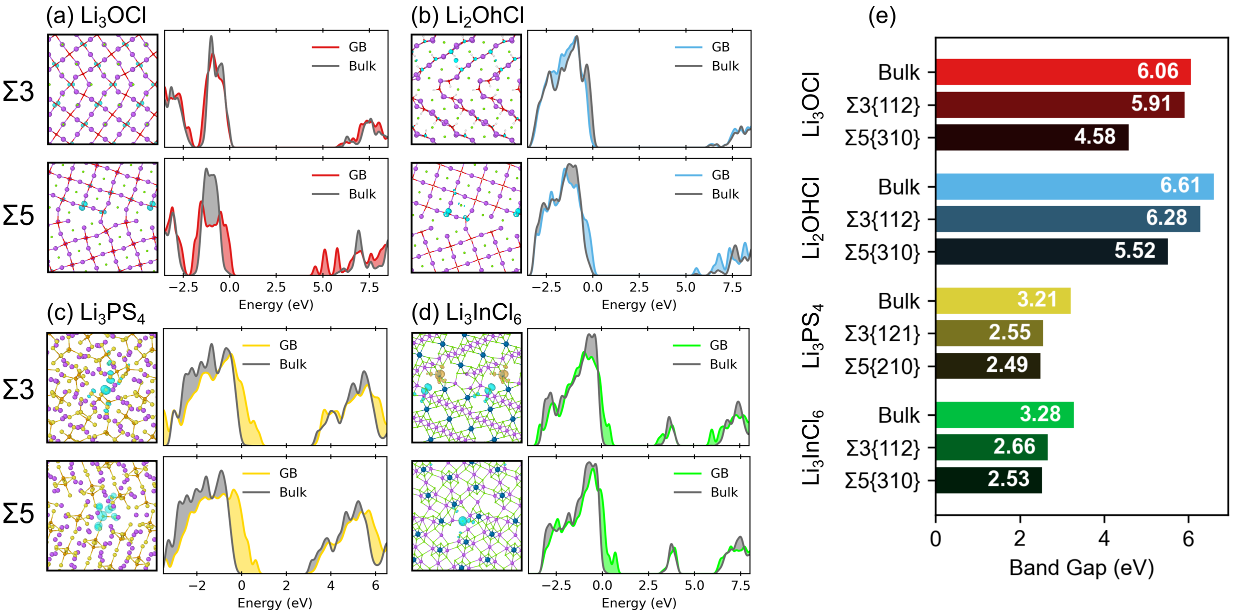

Figure 2: Projected density of states with associated GB structures for (a) Li_3OCl, (b) Li_2OHCl, (c) Li_3PS_4 and (d) Li_3InCl_6. Partial charge density isosurfaces show the highest occupied orbital (turquoise) and, where relevant, the lowest occupied orbital (yellow). In all three materials, the highest occupied molecular orbitals are often localised. (e) Summary of the band gaps of each material in bulk and in the vicinity of the GBs.

Impact on Electronic Structure and Polaron Formation

To determine the influence these GBs have on the electronic properties of the solid electrolytes, we calculated the projected density of states (PDOS) using the hybrid-DFT functional HSE06[29,30] for each GB alongside a bulk-like region in the center of the grain. All of the considered GBs exhibit reduced band gaps in the vicinity of the boundary (Figure 4d), with the change in the Li_3OCl Σ3{112} GB being very small. In general, this corresponds to states appearing above the valence band maximum (VBM), except for in the cases of the Li_3OCl Σ5{310} and Li_3InCl_6 Σ3{112} GBs, where there are significant contributions from states appearing below the conduction band minimum (CBM). Narrowed band gaps may also imply that the GBs contain charge traps in their equilibrium geometry. In order to visualize the band edges, we add an electron and create a hole in each system without optimizing the geometry; the spin density isosurfaces associated with each case show where charge will prefer to localize. Evidence of electron trapping is not especially prevalent; whilst the Li_3InCl_6 $\Sigma3\{112\}$ GB shows some localization of electrons around In sites that form part of the edge-sharing octahedra, the electron density in the Li_3OCl $\Sigma5\{310\}$ is sufficiently diffuse that it does not appear in the isosurface plots. Conversely, evidence of hole trapping is far more pronounced and, in all cases where states appear above the VBM, there are highly localized holes centered on the anions in the vicinity of the GB.

The narrowing of band gaps at GBs represents a challenge in the development of solid electrolytes; an efficient ionic conductor must have poor electrical conductivity, which is achieved by having a wide band gap. Clearly, GBs with a very narrow band gap would have higher electrical conductivity which would encourage leakage current, reducing the efficiency of the device. For example, in the case where the narrowing of the band gap originates from states below the CBM, we would expect free electrons to segregate towards these lower-energy states at the boundary, leading to leakage current being dominated by the higher density of electrons in the GB. This has been shown to contribute to the formation of Li-metal dendrites or 'filaments' along GBs in $Li_7La_3Zr_2O_{12}$,[11] which would eventually lead to the failure of the device. None of the GBs studied here show severely narrowed gaps, and the localized nature of the GB states implies a high effective mass that would not be conducive to electrical conductivity. However, conduction of delocalized charge carriers within bands - as would be seen in a metal or a narrow-gap semiconductor - is not the only means by which electronic conduction takes place.

When an ion can exist in multiple charge states, it is possible that polaron formation can occur. This describes a process whereby a charge carrier induces a polarization in the lattice which, in turn, causes a charge carrier to become trapped on a specific ion as a polaron; the charge carrier has effectively trapped itself. Even though the charge carriers in polarons are highly localized, it is possible for polarons to hop between sites with relatively low barriers,[31–33] which may also contribute to an increase in electrical conductivity along GBs in these materials. In the case of Li_3OCl and Li_3PS_4, the strong hole localization around the ions in the equilibrium geometry indicates that there may be some tendency towards forming polarons where a hole traps on either a O^{2-} or S^{2-} to form a O^- or S^-, respectively; evidence of polaron formation is reported across a wide variety of oxide and sulfide materials[34–37] and previous theoretical studies have shown that polaron trapping can be favourable in the vicinity of GBs.[26,38] Whilst the band edges in Li_2OHCl are localized in a similar manner to Li_3OCl, a polaron formed by trapping a hole on OH^- to form a OH^0 is unlikely to be long-lived. Similarly, in Li_3InCl_6, hole polarons should not be expected to form through a hole trapping on a Cl^- to form a Cl^0, but it may be the case that electrons can trap on In^{3+} to form In^{2+}, which might also contribute to the formation of Li dendrites through the reaction $In^{2+} + Li^+ \rightarrow In^{3+} + Li^0$, for example.

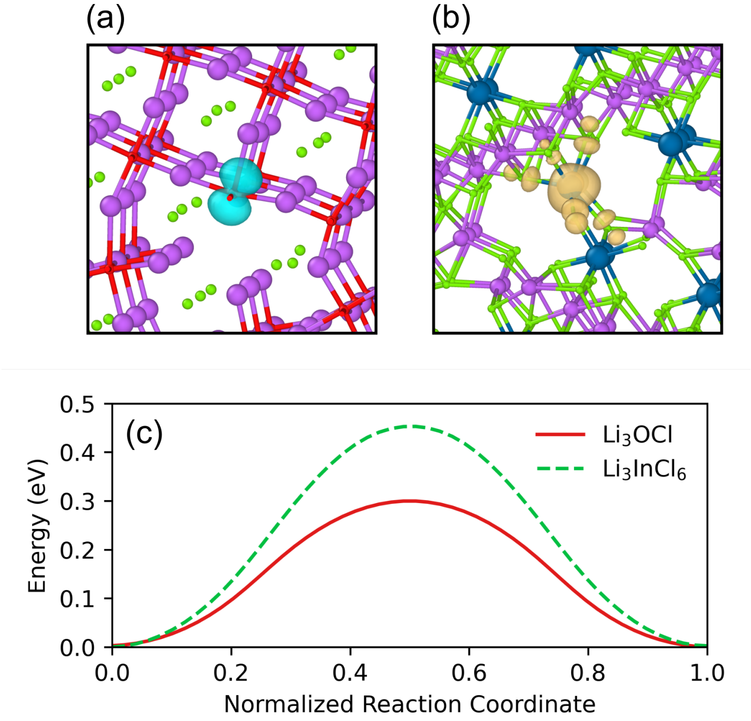

Figure 3: Isosurface plots of the (a) hole polaron in Li_3OCl and (b) electron polaron in Li_3InCl_6. (c) The adiabatic potential energy surface associated with the hopping of each polaron.

In order to determine how large of a role polaron diffusion is likely to play in leakage current at GBs of solid electrolytes, we take the case study of a hole polaron localized at the Li_3OCl $\Sigma3\{310\}$ GB (Figure 3a) and a electron polaron in Li_3InCl_6 $\Sigma3\{112\}$ GB (Figure

3b). The ionization barrier of a polaron can be estimated by calculating the potential energy surface that interpolates between the polaron geometry and the equilibrium geometry corresponding to no trap. We find that neither polaron shows any barrier to trapping, indicating that the formation of these polarons is very favourable and that band-like conduction of their respective charge carriers would be unlikely at these boundaries. Polaron hopping rates can be calculated computationally using Marcus–Emin–Holstein–Austin–Mott (MEHAM) theory.[33,39,40] Essentially, all the information required to calculate polaron hopping rates from MEHAM theory can be obtained from the potential energy surface that interpolates between the geometry corresponding to the initial state and the geometry corresponding to the final state in which a polaron is localized on a neighbouring site; a more complete description can be found in the supplementary information. For the hole polaron in Li_3OCl, we calculate an adiabatic activation energy of 0.30 eV and a 300 K hopping rate of 4.1×10^8 Hz. The electron polaron in Li_3InCl_6 has a higher adiabatic activation energy of 0.45 eV and a correspondingly lower 300 K hopping rate of 6.4×10^5 Hz. Neither of these hopping rates is exceptionally high but, for the hole polaron especially, the rate is comparable that of some of the reported hopping pathways in TiO_2 which is generally considered to be a good polaronic conductor.[33,39,40]

These results highlight important considerations that need to be made when synthesizing solid electrolyte materials. Even in the absence of extrinsic dopants, a material can have free charge carriers due to 'self-doping' by intrinsic defects. For example, a recent study by Gorai et al. predicted that Na_3PS_4 is intrinsically *p*-type due to self-doping by Na vacancies and that argyrodite Li_6PS_5Cl is intrinsically *n*-type due to self-doping by Li interstitials.[21] Then, by analysis of defect energetics, it is determined that higher synthesis temperatures would lead to higher intrinsic conductivity in the bulk of the material due to the higher concentration of the point defects responsible for self-doping. Let us consider the example of intrinsically *p*-type Na_3PS_4. It may be tempting to reduce synthesis temperatures as far as possible to suppress the formation of acceptor defects (to reduce hole concentration and associated conductivity) but lower synthesis temperatures would also lead to smaller grain sizes and increased numbers of GBs. Given the prevalence of states above the VBM across all the materials considered in our study (especially noticeable in the closely-related sulfide Li_3PS_4) we should expect that these GBs would exhibit the levels of high hole conductivity that we would seek to avoid when choosing a low synthesis temperature. It is therefore clear that there is a fine balance between the controlling the relative proportions of point defects and extended defects. In comparison, the intrinsically n-type Li_6PS_5Cl poses a simpler problem; GBs with states above the VBM are less deleterious in an n-type material where there are fewer holes available to fill traps, so lower synthesis temperatures, leading to a larger number of GBs, would not be as much of a concern regarding electronic conductivity.

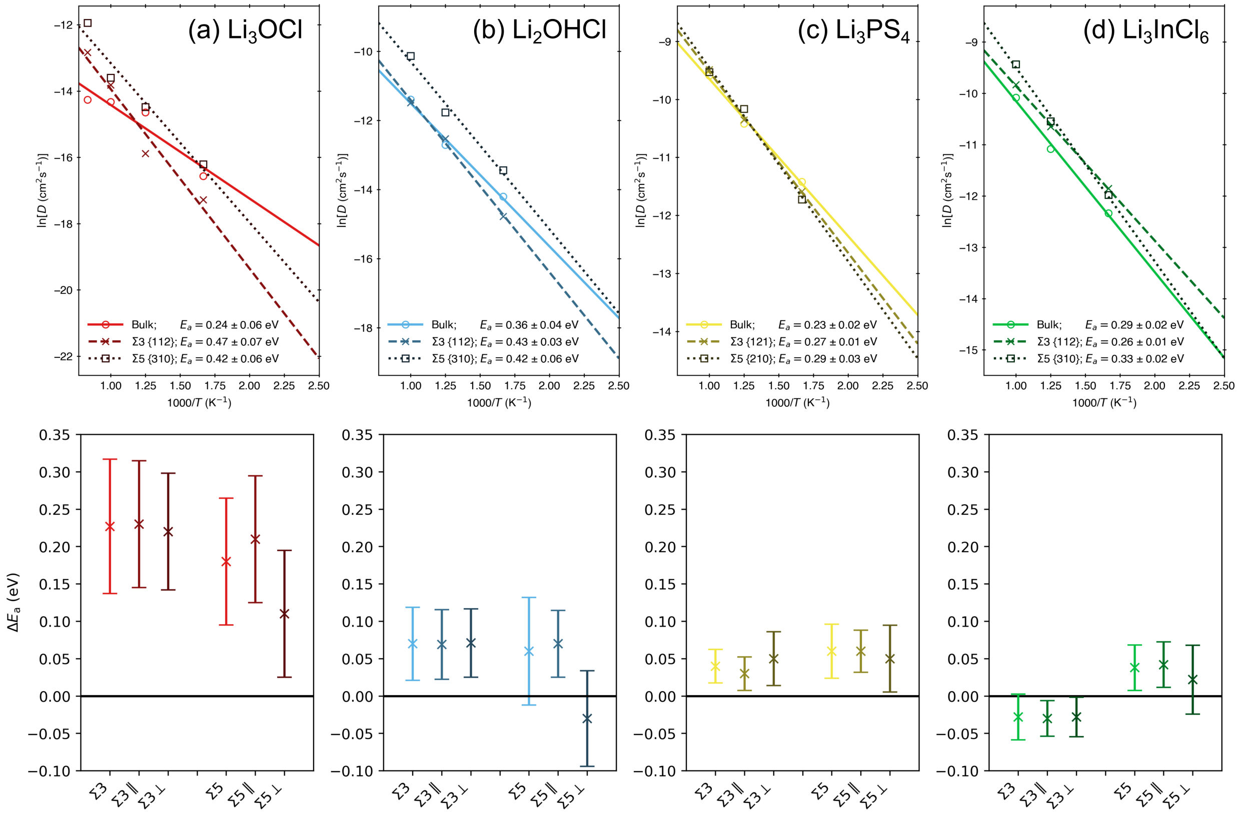

Figure 4: Li-ion diffusivities for the bulk and the GBs of (a) Li_3OCl, (b) Li_2OHCl (c) Li_3PS_4, and (d) Li_3InCl_6. Below each diffusivity plot we also show the relative activation energies in the GBs compared to bulk, $\Delta E_a = E_a^{GB} - E_a^{Bulk}$, associated with total diffusion as well as decomposed into components parallel (∥) and perpendicular (⊥) to the GB plane.

Ion Transport at the Microscale

A full understanding of solid electrolytes requires consideration of their ion dynamics. The activation energy, E_a, and Li diffusivity for each GB system and the bulk of each material was calculated and is shown in Figure 4. Also shown is the relative activation energies in the GBs compared to bulk, $\Delta E_\mathrm{a} = E_\mathrm{a}^\mathrm{GB} - E_\mathrm{a}^\mathrm{Bulk}$, decomposed into components parallel and perpendicular to the GB plane. Aside from the antiperovskite $\Sigma5\{310\}$ GBs, there is not a significant difference in the activation energies through and along the GB planes. In Li_3OCl (Figure 4a), we find that the presence of GBs has a profound effect on Li-ion conductivity, with values of E_a increased by around 0.2 eV in both GB systems, which is in good agreement with previous calculations that employed classical interatomic potentials.[10] This provides further confirmation as to why computational predictions from simulations on bulk tend to overestimate the conductivity of antiperovskite materials compared to experiments which report activation energies as large as 0.6 eV,[23,41] which is in better agreement with our GB simulations than with our bulk simulations. For Li_2OHCl, the increases in activation energy compared to the bulk are far less pronounced (Figure 4b). In the case of $\Sigma5\{310\}$ GB, the activation energy through the GB plane is actually slightly lower than the bulk, though it is offset by an increased activation energy along the GB plane. Again, the systems containing GBs are closer to experimental reports of activation energies in the range 0.5-0.6 eV.[42,43]

In comparison, for Li_3PS_4 (Figure 4c) we find that the presence of GBs has a comparatively minor impact on ionic conduction, with activation energies for the bulk and the GBs ranging between 0.22 and 0.29 eV, which is in excellent agreement with experimentally reported values for crystalline β-Li_3PS_4 of 0.24 eV and 0.27 eV.[44,45] The lower impact of GBs in sulfides compared to oxides has been established previously using classical models and can be attributed to the stronger bonding between the cation and the oxide anion compared the sulfide anion.[16] The behaviour of Li_3InCl_6 GBs has not yet been reported, but we find that it is superior to the behaviour of Li_3PS_4 (Figure 4d), with small changes to E_a of no more than around 0.04 eV. Our predicted activation energies of 0.30-0.34 eV for the GB systems agrees remarkably well with reported experimental activation energies for Li_3InCl_6, which are in the range of around 0.32-0.35 eV.[24,25] Overall, the interfacial diffusion behaviour of Li_3InCl_6 shows an encouraging tolerance towards GBs.

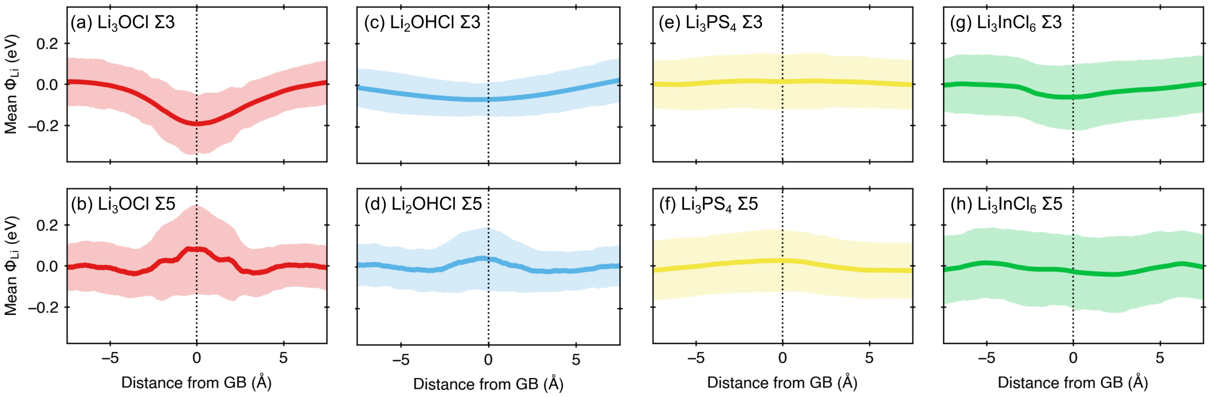

Figure 5: Mean electrostatic potentials around Li ions, ϕ_{Li}, as a function of distance from the GB for the (a) Li_3OCl $\Sigma3\{112\}$, (b) Li_3OCl $\Sigma5\{310\}$ GBs, (c) Li_2OHCl $\Sigma3\{112\}$, (d) Li_2OHCl $\Sigma5\{310\}$, (e) Li_3PS_4 $\Sigma3\{121\}$, (f) Li_3PS_4 $\Sigma5\{210\}$, (g) Li_3InCl_6 $\Sigma3\{112\}$ and (h) Li_3InCl_6 $\Sigma5\{310\}$ GBs. All calculated from 600 K AIMD. Shaded areas show one standard deviation of the calculated mean of ϕ_{Li} at a given distance. Vertical dashed line shows position of GB. For clarity, the mean ϕ_{Li} values have been shifted such that the mean bulk-like value is 0 eV.

An obvious cause for the increase of E_{a} at a GB would be perturbations to the electrostatic potential in the vicinity of the boundary. The segregation of charged defects may lead to the development of a space charge region and a corresponding electrostatic barrier,[27,46,47] but approximating the space charge potential for a given material requires a detailed analysis of defect energetics and is beyond the scope of the current study. Nevertheless, aside from the space-charge region, electrostatic perturbations may arise as a property intrinsic to the GB structure. One method to quantify the effect of the electrostatic potential on an Li ion is to calculate the average electrostatic potential around the ion, which we shall call ϕ_{Li}. The total electrostatic potential experiences large variations due to alternating layers of cations and anions, as well as larger perturbations in the voids of the GBs; focusing on ϕ_{Li} allows us to investigate the effects that the GBs have specifically on the electrostatic environment of the Li ions. We calculated ϕ_{Li} for a sample of 50 frames for each GB AIMD trajectory

(800 K for Li_3OCl and 600 K for Li_2OHCl, Li_3PS_4 and Li_3InCl_6). This value is plotted as the mean of ϕ_{Li} as a function of distance from the boundary (Figure 5). In both of the Li_3OCl GBs, the value of ϕ_{Li} tends to vary significantly in the vicinity of the GBs, with an absolute difference from the bulk value of around 0.20 eV and 0.10 eV for the $\Sigma3\{112\}$ and $\Sigma5\{310\}$ GBs, respectively, which aligns fairly well with the observed changes in E_{a}. In comparison, Li_2OHCl shows a much weaker perturbation to ϕ_{Li}, with Li_3InCl_6 and Li_3PS_4 showing a remarkably flat profile, suggesting that the considered GBs do not have a strong impact on the electrostatic landscape of Li, thereby providing an explanation for the small effect they have on conductivity. The antiperovskite $\Sigma5\{310\}$ GBs both show higher variance in ϕ_{Li} in the vicinity of the GB, which may explain the higher energetic barrier to conductivity along the GB compared to through the GB.

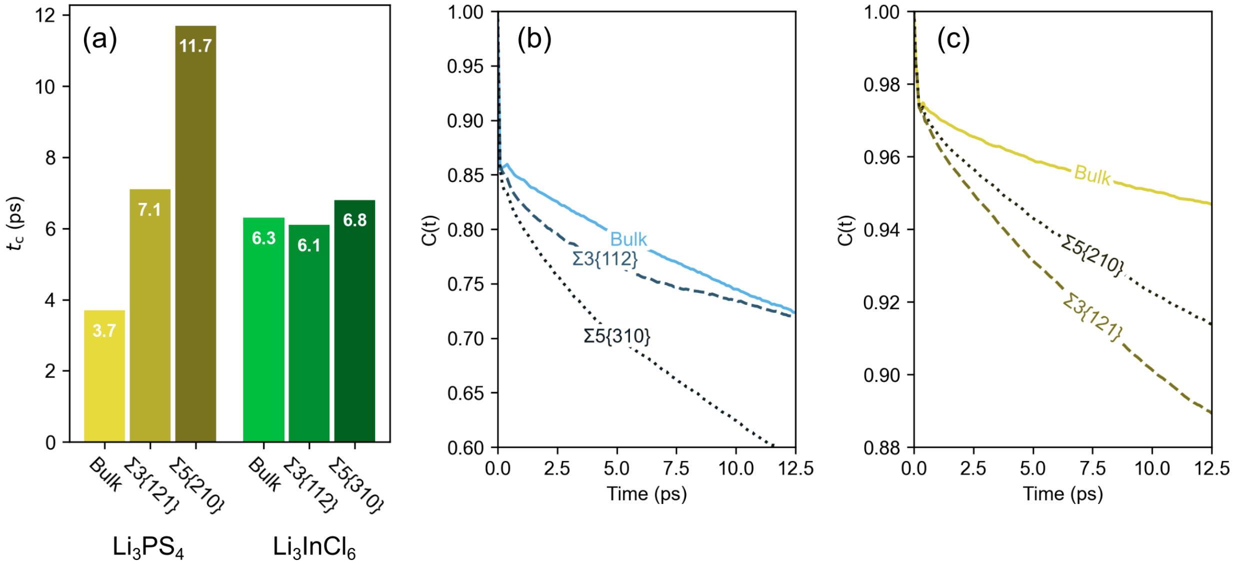

Figure 6: (a) Characteristic timescale of correlation, t_{c}, for the bulk and GBs of Li_3PS_4 and Li_3InCl_6. Vector autocorrelation function, $C(t)$, for the bulk and GBs of (b) Li_3OCl and (c) Li_3PS_4. All displayed quantities have been calculated at 600 K.

The reasons for the stark differences in electrostatic behaviour can, in part, be attributed to the character of the anions. A larger anion will generally more polarizable than a smaller one, and therefore S and Cl will be able to more effectively screen electrostatic perturbations than O can. The OH anion is an interesting case as it differs from O by being a polyanion with a strong dipole which can undergo rotation and reorientation; such rotations would allow the anion to rotate to oppose electric fields created by electrostatic perturbations in the vicinity of the boundary. This reorientation of polyanions is known as the 'paddle-wheel effect',[48,49] and it is known to also occur in Li_3PS_4. The degree of polyanion reorientation occurring in the system can be quantified by calculating the vector reorientation autocorrelation function, $C(t)$, which is defined as

$$C(t) = \langle \mathbf{u}(t+t') \cdot \mathbf{u}(t) \rangle, \tag{1}$$

where $\mathbf{u}(t)$ is a unit vector from the center of mass of the polyanion (O or P) to a covalently-bonded atom (H or S). We observe faster reorientation in the GBs of the Li_2OHCl (Figure 6b), which we propose is due to anions rotating to oppose local perturbations in the electrostatic potential. The GBs in Li_3PS_4 also show greater degrees of reorientation (Figure 6c), which may act in tandem with the larger S ion to screen electric fields, though the PS_4 polyanion does not have as strong a dipole as OH.

Even if the degree of concerted motion is not increased by faster reorientation, it might be expected that diffusivity along to the GB plane is faster than diffusivity through the GB. However, we find that the difference in activation energy parallel and perpendicular to the GB plane is rather small (Figure 4c). The paddle-wheel effect has also been proposed to enable concerted motion.[48] By calculating the distinct part of the van Hove correlation function, $G_\mathrm{d}(\mathbf{r}, t)$, at 800 K for Li_3OCl and 600 K for Li_3PS_4 and Li_3InCl_6 (Figure S4), we can determine a characteristic timescale of correlation in each of the systems, t_c, which we define in this work as the lowest value of t for which $G_\mathrm{d}(0, t) > 2$. For context, using this metric, previous AIMD simulations carried out on a selection of 'best-in-class' super-ionic conductors - namely, $Li_{10}GeP_2S_{12}$, $Li_7La_3Zr_2O_{12}$, and $Li_{1.3}Al_{0.3}Ti_{1.7}(PO_4)_3$ - yield values of around $t_\mathrm{c} < 1.0$ ps.[50] None of the materials considered in this study exhibit such highly-correlated motion, but nonetheless provide a valuable case study.

The value of t_c is calculated for Li_3OCl at 800 K, and Li_3PS_4 and Li_3InCl_6 at 600 K. Transport in the bulk of Li_3OCl does not exhibit strong correlation, with a large value of

$t_\mathrm{c} = 8.9$ ps. For both the $\Sigma3\{112\}$ and $\Sigma5\{310\}$ GBs, the timescale of correlation is vastly increased to far beyond the 15 ps time window for which we have calculated $G_\mathrm{d}(\mathbf{r}, t)$ (see Supplementary Information Figure 4). Li_2OHCl also shows little correlated motion, with neither the bulk nor either GB having a correlation timescale within the 15 ps window. In Li_3PS_4, we see much more strongly correlated motion in the bulk of the material with $t_\mathrm{c} = 3.7$ ps, with the $\Sigma3\{121\}$ and $\Sigma5\{210\}$ GBs having increased correlation timescales of around 7.1 ps and 11.7 ps, respectively. For bulk Li_3InCl_6, we find a higher correlation timescale of 6.3 ps, sitting roughly in the middle of of bulk Li_3PS_4 and Li_3OCl, but the presence of GBs has no real impact on t_c, with the $\Sigma3\{112\}$ and $\Sigma5\{310\}$ GBs having timescales of around 6.1 ps and 6.8 ps, respectively (Figure 6a), which is perhaps not surprising given the lack of impact the GBs have on diffusivity at these temperatures.

Clearly, increased polyanion reorientation at the GBs in Li_3PS_4 is not increasing diffusivity beyond what would be seen in the bulk. The radial distribution functions (RDF) provides some insight. The GBs in Li_3PS_4 are less crystalline than the bulk, evidenced by the much broader and less-defined peaks in the P-P peaks (Supplementary Information), but despite this, the Li-S and Li-Li RDFs are strikingly similar to the bulk. This suggests that the increased reorientation is not enabling greater concerted motion or diffusivity, but that the reorientation is acting to maintain a similar coordination environment for Li, which help to flatten the potential energy surface that the Li travels along. Experimentally, samples of Li_3PS_4 prior to calcining and sintering to produce a highly-crystalline material, exhibit significant amorphous regions without significant loss of conductivity.[45] We propose that the good conductivity in low-crystallinity regions - whether that is in amorphous regions or in the vicinity of GBs - may be attributable to fast reorientation allowing Li to maintain a favourable coordination environment even in a disordered structure. In comparison, the RDFs for the Li_3InCl_6 GBs diverge more significantly from the bulk. The changes are primarily reflected in a lower degree of Li-Li coordination enabled by the more disordered structure; lowered Li-Li interactions is likely part of the reason that diffusion is more facile in these boundaries.

Conclusions

The structural, electronic and ion transport properties of GBs are pivotal to the design of solid electrolytes for solid-state batteries. Despite this fact, our understanding of GBs in these materials is restricted by the current limitations facing both experimental and computational methods. In this study, we have investigated the significant effects that GBs have on four representative solid electrolyte materials (Li_3OCl, Li_2OHCl, Li_3PS_4 and Li_3InCl_6) using first-principles simulations for the first time. The key results and associated design principles are summarized as follows:

1. It is found that for all four materials, GBs lead to reductions in the band gap, sometimes with the appearance of highly-localized trap states for electrons or holes. Polarons formed at the boundary can hop with relatively low barriers, leading to increased electronic conductivity. Incorporating ions that are less likely to change charge state would mitigate this behavior.

2. The GBs in Li_3OCl are found to lead to a severe reduction in Li-ion conductivity. In contrast, the GBs in Li_2OHCl and Li_3PS_4 are less severe, with Li_3InCl_6 having particularly negligible effects on activation energy. This can, in part, be attributed to the GBs in these materials not significantly perturbing the electrostatic potential. Incorporating ions with higher polarizabilty or the ability to oppose electric fields by reorienting would mitigate the deleterious effects of electrostatic perturbations.

3. In the case of Li_3PS_4, GBs also lead to an increased degree of reorientation by polyanions. Our simulations reveal that GBs have a significant effect on the timescale of the correlation of Li-ion diffusion in solid electrolytes even where the diffusivity is relatively unaffected. Incorporated polyanions able to undergo reorientation can act to maintain coordination environments in the vicinity of the GB, enabled more facile diffusion.

By considering a range of materials simultaneously, these atomistic insights highlight a variety of important considerations that must be made when designing solid electrolyte materials. We propose that future studies should focus more on detailed investigations into the specific mechanisms that have been hinted at here, for example charge trapping or complex polyanionic motion at GBs and other important interfaces. Augmenting our fundamental understanding of these interfaces and their complex influence is crucial for the future development of solid electrolytes for solid-state batteries.

Computational Methods

We model GBs in a periodic supercell containing two grains of finite width brought into contact to produce two symmetrically-equivalent GBs. We ensure that the grains in each model are at least 15 Å thick in order to minimize interactions between the grains. To determine low-energy GB structures, we performed a systematic scan over all possible rigid-body translations between the grains, with the translation steps taken to be as close to 0.5 Å as possible whilst allowing the resulting grid of translations to be commensurate with the lattice vectors parallel to the GB plane. The structure with the lowest energy is determined to be a stable structure, where the formation energy, γ, in a periodic supercell is given by

$$\gamma = \frac{E_{\mathrm{tot}}[\mathrm{GB}] - NE_{\mathrm{Bulk}}[\mathrm{GB}]}{2A}, \tag{2}$$

where $E_{\mathrm{tot}}[\mathrm{GB}]$ is the total energy of a GB supercell, N is the total number of units of bulk, $E_{\mathrm{tot}}[\mathrm{Bulk}]$ is the total energy of a unit of bulk and A is the cross-sectional area of the slab where the factor of two accounts for the two equivalent interfaces in the model. This procedure has been used extensively in previous studies to successfully predict GB structures.[26–28,51]

All geometry optimizations, AIMD and electronic structure calculations were carried out using the implementation of DFT within CP2K.[52] Geometry optimization is performed until the force on ions is less than 0.01 eV $Å^{-1}$. When optimizing GB geometries, lattice vectors parallel to the GB are held fixed and the lattice vector normal to the GB is allowed to relax. Our choice of exchange-correlation functional for standard calculations is PBEsol,[53] which generally performs well for solids. We use double-ζ basis sets optimized from molecular calculations (MOLOPT)[54] and Goedecker-Teter-Hutter pseudopotentials available within CP2K.[55–57] We use five multigrids with a relative cutoff of 50 Ry and the finest grid having a cutoff of 500 Ry. CP2K is highly efficient when sampling only the Γ-point, so it is necessary to converge the size of the supercell in order to achieve proper reciprocal space sampling. For Li_3OCl we find a supercell of 320 atoms yields lattice parameters of $a = b = c = 3.86$ Å. For Li_3PS_4 we find a supercell of 384 atoms yields lattice parameters of of $a = 6.11$ Å, $b = 8.01$ Å and $a = 12.98$ Å. For Li_3InCl_6 a supercell of 360 atoms yields lattice parameters of $a = 6.45$ Å, $b = 11.05$ Å, $c = 6.36$ Å and $\beta = 111.1°$. The parameters for each material are in good agreement with reported experimental results.[22,25,58] For the PDOS and partial charge density plots at each of the GBs, we use hybrid DFT functional HSE06[29,30] to improve the band gaps and charge localization. The computational cost of hybrid calculations is reduced by the CP2K implementation of the auxiliary density matrix method (ADMM)[59,60] in which exchange integrals are approximated through mapping onto smaller, more localized basis sets.

All AIMD calculations were carried for at least 100 ps (with the exception of Li_2OHCl, which used a smaller time step and ran for at least 80 ps) using the NVT ensemble with a Nosé-Hoover thermostat. Simulations were ran at temperatures of 600 K, 800 K, and 1000 K for Li_2OHCl, Li_3PS_4 and Li_3InCl_6, and at elevated temperatures of 600 K, 800 K, 1000 K, and 1200 K for Li_3OCl due to the low levels of diffusion observed at the GBs in this material. A timestep of 2 ps was used for the Li_3OCl, Li_3PS_4 and Li_3InCl_6 and a timestep of 1 ps was used for the Li_2OHCl. Self-diffusion data for the Li ions were calculated according to

$$\langle r_i^2(t) \rangle = 6 D_{\mathrm{Li}} t, \tag{3}$$

where $\langle r_i^2(t) \rangle$ is the mean squared displacement, D_{Li} is the Li diffusion coefficient and t is time. Mean squared displacements are calculated using the smoothing method implemented in Pymatgen's diffusion analysis modules.[61] These values can then be converted to conductivities, σ, using the Nernst-Einstein equation

$$\sigma = \frac{nq^2}{kT} D_{\mathrm{Li}}, \tag{4}$$

where n is the number density of Li, q is the charge of Li, k is the Boltzmann constant, and T is the temperature. Li ion vacancies are introduced into the systems at a concentration of 5% in order to encourage ionic mobility where the charge is balanced by introducing a corresponding number of anion defects. Analysis of the trajectories was carried out using the TRAVIS code.[62,63]

Acknowledgement

The authors gratefully acknowledge EPSRC for funding via EP/V013130/1. JAD gratefully acknowledges Newcastle University for funding through a Newcastle Academic Track (NUAcT) Fellowship. Via membership of the UK's HEC Materials Chemistry Consortium, which is funded by the EPSRC (EP/R029431), this work used the ARCHER2 UK National Supercomputing Service.

Supporting Information Available

Description of the theory of polaron hopping rates. Plots of the radial distribution function and distinct part of the Van Hove correlation function.

References

(1) Famprikis, T.; Canepa, P.; Dawson, J. A.; Islam, M. S.; Masquelier, C. Fundamentals of Inorganic Solid-State Electrolytes for Batteries. *Nat. Mater.* **2019**, *18*, 1278–1291.

(2) Janek, J.; Zeier, W. A solid future for battery development. *Nature Energy* **2016**, *1*, 16141.

(3) Bachman, J. C.; Muy, S.; Grimaud, A.; Chang, H.-H.; Pour, N.; Lux, S. F.; Paschos, O.; Maglia, F.; Lupart, S.; Lamp, P.; Giordano, L.; Shao-Horn, Y. Inorganic Solid-State Electrolytes for Lithium Batteries: Mechanisms and Properties Governing Ion Conduction. *Chemical Reviews* **2016**, *116*, 140–162, PMID: 26713396.

(4) Zhang, Z.; Shao, Y.; Lotsch, B.; Hu, Y.-S.; Li, H.; Janek, J.; Nazar, L. F.; Nan, C.-W.; Maier, J.; Armand, M.; Chen, L. New horizons for inorganic solid state ion conductors. *Energy Environ. Sci.* **2018**, *11*, 1945–1976.

(5) Zhao, Q.; Stalin, S.; Zhao, C.-Z.; Archer, L. A. Designing solid-state electrolytes for safe, energy-dense batteries. *Nature Reviews Materials* **2020**, *5*, 229–252.

(6) Hong, M.; Dong, Q.; Xie, H.; Clifford, B. C.; Qian, J.; Wang, X.; Luo, J.; Hu, L. Ultrafast Sintering of Solid-State Electrolytes with Volatile Fillers. *ACS Energy Lett.* **2021**, *6*, 3753–3760.

(7) Wei, R.; Chen, S.; Gao, T.; Liu, W. Challenges, Fabrications and Horizons of Oxide Solid Electrolytes for Solid-State Lithium Batteries. *Nano Select* **2021**, *2*, 2256–2274.

(8) Liu, Z.; Fu, W.; Payzant, E. A.; Yu, X.; Wu, Z.; Dudney, N. J.; Kiggans, J.; Hong, K.; Rondinone, A. J.; Liang, C. Anomalous High Ionic Conductivity of Nanoporous β-Li_3PS_4. *J. Amer. Chem. Soc.* **2013**, *135*, 975–978.

(9) Sasano, S.; Ishikawa, R.; Sánchez-Santolino, G.; Ohta, H.; Shibata, N.; Ikuhara, Y.

Atomistic Origin of Li-Ion Conductivity Reduction at $(Li_{3x}La_{2/3-x})TiO_3$ Grain Boundary. *Nano Lett.* **2021**, *21*, 6282–6288.

(10) Dawson, J. A.; Canepa, P.; Famprikis, T.; Masquelier, C.; Islam, M. S. Atomic-Scale Influence of Grain Boundaries on Li-ion Conduction in Solid Electrolytes for All-Solid-State Batteries. *J. Amer. Chem. Soc.* **2018**, *140*, 362–368.

(11) Liu, X.; Garcia-Mendez, R.; Lupini, A. R.; Cheng, Y.; Hood, Z. D.; Han, F.; Sharafi, A.; Idrobo, J. C.; Dudney, N. J.; Wang, C., et al. Local Electronic Structure Variation Resulting in Li 'Filament' Formation Within Solid Electrolytes. *Nat. Mater.* **2021**, 1–6.

(12) Cheng, E. J.; Sharafi, A.; Sakamoto, J. Intergranular Li Metal Propagation Through Polycrystalline $Li_{6.25}Al_{0.25}La_3Zr_2O_{12}$ ceramic electrolyte. *Electrochim. Acta* **2017**, *223*, 85–91.

(13) Kahle, L.; Marcolongo, A.; Marzari, N. High-throughput Computational Screening for Solid-State Li-ion Conductors. *Energy Environ. Sci.* **2020**, *13*, 928–948.

(14) Knauth, P. Inorganic Solid Li Ion Conductors: An Overview. *Solid State Ion.* **2009**, *180*, 911–916.

(15) Meesala, Y.; Jena, A.; Chang, H.; Liu, R.-S. Recent Advancements in Li-ion Conductors for All-Solid-State Li-ion Batteries. *ACS Energy Lett.* **2017**, *2*, 2734–2751.

(16) Dawson, J. A.; Canepa, P.; Clarke, M. J.; Famprikis, T.; Ghosh, D.; Islam, M. S. Toward Understanding the Different Influences of Grain Boundaries on Ion Transport in Sulfide and Oxide Solid Electrolytes. *Chem. Mater.* **2019**, *31*, 5296–5304.

(17) Dawson, J. A.; Islam, M. S. A Nanoscale Design Approach for Enhancing the Li-Ion Conductivity of the $Li_{10}GeP_2S_{12}$ Solid Electrolyte. *ACS Mater. Lett.* **2022**, *4*, 424–431.

(18) Yu, S.; Siegel, D. J. Grain Boundary Contributions to Li-Ion Transport in the Solid Electrolyte Li7La3Zr2O12 (LLZO). *Chemistry of Materials* **2017**, *29*, 9639–9647.

(19) Nakano, K.; Tanibata, N.; Takeda, H.; Kobayashi, R.; Nakayama, M.; Watanabe, N. Molecular Dynamics Simulation of Li-Ion Conduction at Grain Boundaries in NASICON-Type LiZr2(PO4)3 Solid Electrolytes. *The Journal of Physical Chemistry C* **2021**, *125*, 23604–23612.

(20) Heo, T. W.; Grieder, A.; Wang, B.; Wood, M.; Hsu, T.; Akhade, S. A.; Wan, L. F.; Chen, L.-Q.; Adelstein, N.; Wood, B. C. Microstructural impacts on ionic conductivity of oxide solid electrolytes from a combined atomistic-mesoscale approach. *npj Computational Materials* **2021**, *7*.

(21) Gorai, P.; Famprikis, T.; Singh, B.; Stevanovic, V.; Canepa, P. Devil is in the Defects: Electronic Conductivity in Solid Electrolytes. *Chem. Mater.* **2021**, *33*, 7484–7498.

(22) Zhao, Y.; Daemen, L. L. Superionic Conductivity in Lithium-Rich Anti-Perovskites. *J. Amer. Chem. Soc.* **2012**, *134*, 15042–15047.

(23) Dawson, J. A.; Famprikis, T.; Johnston, K. E. Anti-perovskites for solid-state batteries: recent developments, current challenges and future prospects. *J. Mater. Chem. A* **2021**, *9*, 18746–18772.

(24) Li, X.; Liang, J.; Luo, J.; Banis, M. N.; Wang, C.; Li, W.; Deng, S.; Yu, C.; Zhao, F.; Hu, Y., et al. Air-Stable Li_3InCl_6 Electrolyte with High Voltage Compatibility for All-Solid-State Batteries. *Energy Environ. Sci.* **2019**, *12*, 2665–2671.

(25) Li, X.; Liang, J.; Chen, N.; Luo, J.; Adair, K. R.; Wang, C.; Banis, M. N.; Sham, T.-K.; Zhang, L.; Zhao, S., et al. Water-Mediated Synthesis of a Superionic Halide Solid Electrolyte. *Angew. Chem.* **2019**, *131*, 16579–16584.

(26) Quirk, J. A.; Lazarov, V. K.; McKenna, K. P. Electronic Properties of {112} and {110} Twin Boundaries in Anatase TiO_2. *Adv. Theory Simul* **2019**, *2*, 1900157.

(27) Quirk, J. A.; Miao, B.; Feng, B.; Kim, G.; Ohta, H.; Ikuhara, Y.; McKenna, K. P. Unveiling the Electronic Structure of Grain Boundaries in Anatase with Electron Microscopy and First-Principles Modeling. *Nano Lett.* **2021**, *21*, 9217–9223.

(28) Imaeda, M.; Mizoguchi, T.; Sato, Y.; Lee, H.-S.; Findlay, S. D.; Shibata, N.; Yamamoto, T.; Ikuhara, Y. Atomic structure, electronic structure, and defect energetics in $[001](310)\ensuremath{\Sigma}5$ grain boundaries of ${\text{SrTiO}}_{3}$ and ${\text{BaTiO}}_{3}$. *Phys. Rev. B* **2008**, *78*, 245320, Publisher: American Physical Society.

(29) Heyd, J.; Scuseria, G. E.; Ernzerhof, M. Hybrid Functionals Based on a Screened Coulomb Potential. *J. Chem. Phys.* **2003**, *118*, 8207–8215.

(30) Krukau, A. V.; Vydrov, O. A.; Izmaylov, A. F.; Scuseria, G. E. Influence of the Exchange Screening Parameter on the Performance of Screened Hybrid Functionals. *J. Chem. Phys* **2006**, *125*, 224106.

(31) Ellis, B.; Perry, L. K.; Ryan, D. H.; Nazar, L. Small Polaron hopping in Li_xFePO_4 Solid Solutions: Coupled Lithium-ion and Electron Mobility. *J. Amer. Chem. Soc.* **2006**, *128*, 11416–11422.

(32) Emin, D.; Seager, C.; Quinn, R. K. Small-Polaron Hopping Motion in Some Chalcogenide Glasses. *Phys. Rev. Lett.* **1972**, *28*, 813.

(33) Hole Polaron Migration in Bulk Phases of TiO2 Using Hybrid Density Functional Theory. *J. Phys. Chem. C 125*.

(34) Elmaslmane, A. R. Localised Electronic States in Model Systems and Semiconductors. Ph.D. thesis, University of York, 2019.

(35) Cline, R. P.; Utterback, J. K.; Strong, S. E.; Dukovic, G.; Eaves, J. D. On the Nature of Trapped-Hole States in CdS Nanocrystals and the Mechanism of Their Diffusion. *J. Phys. Chem. Lett.* **2018**, *9*, 3532–3537.

(36) Vysochanskii, Y.; Molnar, A.; Yevych, R.; Glukhov, K.; Medulych, M. Ferroelectricity and Polarons in $Sn_2P_2S_6$ Crystals. *Ferroelectrics* **2012**, *440*, 31–41.

(37) Liu, Z.; Balbuena, P. B.; Mukherjee, P. P. Hole Polaron Diffusion in the Final Discharge Product of Lithium–Sulfur Batteries. *J. Phys. Chem. C* **2017**, *121*, 17169–17175.

(38) Wallace, S. K.; McKenna, K. P. Grain Boundary Controlled Electron Mobility in Polycrystalline Titanium Dioxide. *Adv. Mater. Interfaces* **2014**, *1*, 1400078.

(39) Deskins, N. A.; Dupuis, M. Electron transport via polaron hopping in bulk \$\mathrm{Ti}{\mathrm{O}}_{2}\$: A density functional theory characterization. *Phys. Rev. B* **2007**, *75*, 195212, Publisher: American Physical Society.

(40) Deskins, N. A.; Dupuis, M. Intrinsic Hole Migration Rates in TiO2 from Density Functional Theory. *J. Phys. Chem. C* **2009**, *113*, 346–358, Publisher: American Chemical Society.

(41) Xia, W.; Zhao, Y.; Zhao, F.; Adair, K.; Zhao, R.; Li, S.; Zou, R.; Zhao, Y.; Sun, X. Antiperovskite Electrolytes for Solid-State Batteries. *Chemical Reviews* **2022**, *122*.

(42) Hood, Z. D.; Wang, H.; Samuthira Pandian, A.; Keum, J. K.; Liang, C. Li2OHCl Crystalline Electrolyte for Stable Metallic Lithium Anodes. *J. Am. Chem. Soc.* **2016**, *138*, 1768–1771, Publisher: American Chemical Society.

(43) Wang, F.; Evans, H. A.; Kim, K.; Yin, L.; Li, Y.; Tsai, P.-C.; Liu, J.; Lapidus, S. H.; Brown, C. M.; Siegel, D. J.; Chiang, Y.-M. Dynamics of Hydroxyl Anions Promotes Lithium Ion Conduction in Antiperovskite Li2OHCl. *Chem. Mater.* **2020**, *32*, 8481–8491, Publisher: American Chemical Society.

(44) Stöffler, H.; Zinkevich, T.; Yavuz, M.; Senyshyn, A.; Kulisch, J.; Hartmann, P.; Adermann, T.; Randau, S.; Richter, F. H.; Janek, J., et al. Li^+-Ion Dynamics in β-Li_3PS_4 Observed by NMR: Local Hopping and Long-Range Transport. *J. Phys. Chem. C* **2018**, *122*, 15954–15965.

(45) Stöffler, H.; Zinkevich, T.; Yavuz, M.; Hansen, A.-L.; Knapp, M.; Bednarcik, J.; Randau, S.; Richter, F. H.; Janek, J.; Ehrenberg, H., et al. Amorphous Versus Crystalline Li_3PS_4: Local Structural Changes During Synthesis and Li Ion Mobility. *J. Phys. Chem. C* **2019**, *123*, 10280–10290.

(46) Usler, A. L.; De Souza, R. A. A Critical Examination of the Mott–Schottky Model of Grain-Boundary Space-Charge Layers in Oxide-Ion Conductors. *J. Electrochem. Soc.* **2021**, *168*, 056504.

(47) De Souza, R. A. The Formation of Equilibrium Space–Charge Zones at Grain Boundaries in the Perovskite Oxide $SrTiO_3$. *Phys. Chem. Chem. Phys.* **2009**, *11*, 9939–9969.

(48) Smith, J. G.; Siegel, D. J. Low-temperature Paddlewheel Effect in Glassy Solid Electrolytes. *Nature Commun.* **2020**, *11*, 1–11.

(49) Kaup, K.; Zhou, L.; Huq, A.; Nazar, L. F. Impact of the Li Substructure on the Diffusion Pathways in Alpha and Beta Li_3PS_4: an in Situ High Temperature Neutron Diffraction Study. *J. Mater. Chem. A* **2020**, *8*, 12446–12456.

(50) He, X.; Zhu, Y.; Mo, Y. Origin of Fast Ion Diffusion in Super-Ionic Conductors. *Nat. Commun.* **2017**, *8*, 1–7.

(51) McKenna, K. P. Structure, Electronic Properties, and Oxygen Incorporation/Diffusion Characteristics of the $\Sigma5$ TiN (310)[001] Tilt Grain Boundary. *J. Appl. Phys.* **2018**, *123*, 075301.

(52) VandeVondele, J.; Krack, M.; Mohamed, F.; Parrinello, M.; Chassaing, T.; Hutter, J. Quickstep: Fast and Accurate Density Functional Calculations Using a Mixed Gaussian and Plane Waves Approach. *Comput. Phys. Commun.* **2005**, *167*, 103–128.

(53) Perdew, J. P.; Ruzsinszky, A.; Csonka, G. I.; Vydrov, O. A.; Scuseria, G. E.; Constantin, L. A.; Zhou, X.; Burke, K. Restoring the Density-Gradient Expansion for Exchange in Solids and Surfaces. *Phys. Rev. Lett.* **2008**, *100*, 136406.

(54) VandeVondele, J.; Hutter, J. Gaussian Basis Sets for Accurate Calculations on Molecular Systems in Gas and Condensed Phases. *J. Chem. Phys.* **2007**, *127*, 114105.

(55) Krack, M. Pseudopotentials for H to Kr Optimized for Gradient-Corrected Exchange-Correlation Functionals. *Theor. Chem. Acc.* **2005**, *114*, 145–152.

(56) Goedecker, S.; Teter, M.; Hutter, J. Separable Dual-space Gaussian Pseudopotentials. *Phys. Rev. B* **1996**, *54*, 1703.

(57) Hartwigsen, C.; Gœdecker, S.; Hutter, J. Relativistic Separable Dual-Space Gaussian Pseudopotentials From H to Rn. *Phys. Rev. B* **1998**, *58*, 3641.

(58) Homma, K.; Yonemura, M.; Kobayashi, T.; Nagao, M.; Hirayama, M.; Kanno, R. Crystal Structure and Phase Transitions of the Lithium Ionic Conductor Li_3PS_4. *Solid State Ion.* **2011**, *182*, 53–58.

(59) Guidon, M.; Hutter, J.; VandeVondele, J. Robust Periodic Hartree-Fock Exchange for Large-Scale Simulations Using Gaussian Basis Sets. *J. Chem. Theory Comput.* **2009**, *5*, 3010–3021.

(60) Guidon, M.; Hutter, J.; VandeVondele, J. Auxiliary Density Matrix Methods for Hartree-Fock Exchange Calculations. *J. Chem. Theory Comput.* **2010**, *6*, 2348–2364.

(61) Deng, Z.; Zhu, Z.; Chu, I.-H.; Ong, S. P. Data-Driven First-Principles Methods for the

Study and Design of Alkali Superionic Conductors. *Chem. Mater.* **2017**, *29*, 281–288, Publisher: American Chemical Society.

(62) Brehm, M.; Thomas, M.; Gehrke, S.; Kirchner, B. TRAVIS - A Free Analyzer and Visualizer for Monte Carlo and Molecular Dynamics Trajectories. *J. Chem. Phys.* **2011**, *51*, 2007–2023.

(63) Brehm, M.; Thomas, M.; Gehrke, S.; Kirchner, B. TRAVIS — A Free Analyzer for Trajectories from Molecular Simulation. *J. Chem. Phys.* **2020**, *152*, 164105.